

中红外宽带消色差超透镜的设计

张悦^{1,2}, 牟达^{1,2,3*}, 谢蕙阳^{1,2}, 夏鹏宇^{1,2}, 李堂玥^{1,2,3}, 李浩翔^{1,2,3}, 张文瀚^{1,2}¹长春理工大学光电工程学院光电测控与光信息传输技术教育部重点实验室, 吉林 长春 130022;²长春理工大学光电工程学院光电工程国家级教学示范中心, 吉林 长春 130022;³长春理工大学中山研究院, 广东 中山 528400

摘要 中红外热成像系统是通过探测物体本身的辐射进行成像,不需要外部光源。而传统的中红外热成像系统体积大,不利于小型化。本文基于传输相位理论,采用时域有限差分(FDTD)法,使用FDTD软件计算仿真,探究了不同的单元半径、纳米柱高度及单元周期对相位延迟及透过率的影响,并且针对不同的纳米柱半径,利用传输相位调控实现中红外(3~5 μm)波长下全介质硅材料的宽带消色差超透镜设计。其数值孔径为0.24,仿真焦距值为147.3 μm,半峰全宽(FWHM)为8.11 μm,透镜透过率达到70%。设计的超透镜不仅体积小、质量轻、全波长聚焦效率可达到54%,而且为平面透镜,因此易于光学系统集成,在红外成像、红外夜视仪、红外遥感等技术中展现出广阔的应用前景。

关键词 超透镜; 中红外波段; 平面透镜; 消色差; 宽带

中图分类号 O436

文献标志码 A

DOI: 10.3788/AOS231010

1 引言

超表面在平面光学领域被广泛应用^[1],因为其可以在亚波长尺寸下调控入射光波的相位,如今已经应用在光束发生器^[2]、全息成像^[3]、光束整形^[4]等方面。而超透镜是能够进行聚焦的超表面,产生的光波具有双曲相位特征,并且能够提供比传统透镜大的衍射效率。与传统透镜利用调整材料厚度在空间上实现聚焦功能不同,超透镜可以在平面内调控入射光的相位分布。且与传统透镜相比,超透镜极大地减小了系统的体积,同时超透镜也易于集成在其他元件上。但是,在应用中由于材料自身的属性会产生较大的色差,因此,消除色差的影响是超透镜应用中必不可少的一环。

超透镜通过对入射光的相位进行调控实现聚焦功能,当波长变化时,相位随之改变,进而产生色差。由于超透镜不存在球差,因此色差是成像中最主要的像差来源。目前,越来越多的研究人员聚焦于实现消色差超透镜设计。2015年,Capasso课题组的Aieta等^[5]利用介质耦合共振单元设计了一种可以工作在几个离散波长下轴向焦距漂移极小的一维消色差超透镜。之后,Arbabi等^[6]将这一研究扩展至二维平面,实现了工作在915 nm和1550 nm两个离散波长下的二维消色差超透镜,经实验测量,这两个波长下超透镜的聚焦效率分别为22%和65%。2017年,Avayu等^[7]通过使用

Ag、Au、Al三种金属采用密集垂直叠加的方式,设计了能够在可见光波段实现消色差功能的超透镜,但由于金属损耗,其聚焦效率仅有5.8%~8.7%。Li等^[8]应用空间复用光调制技术,利用几何相位理论设计了可见光分离波长消色差超透镜。2018年,Wang等^[9]设计了超透镜的不同结构参数,实现了400~660 nm波长的宽带消色差。李阳等^[10]运用补偿超透镜结构色散和材料自身色散,在波长1000~2000 nm范围内实现了消色差的功能。Ndao等^[11]利用渔网式结构的超透镜,展示了波长从可见光(640 nm)至红外(1200 nm)超长带宽的消色差。陈玮婷等^[12]将超透镜的单元结构设计为类纳米柱结构以此进行反射式的消色差。通过应用几何相位理论排列单元结构,以达到对电磁波相位、群时延和色散的控制,实现了在波长1200~1680 nm范围内的消色差。同时,王书明等^[13]应用传输相位理论,通过分区域设计不同形状的纳米柱结构,同样实现了波长在1200~1680 nm范围内的消色差设计。随后,2021年,美国肯塔基大学的Balli团队^[14]使用悬浮于相板上的高对称的圆柱实现了450~1700 nm的消色差聚焦,聚焦效率进一步提高到60%左右。2022年,Xiong等^[15]通过使用特殊设计的交叉单元结构进行相位补偿,在3~5 μm的宽带波长范围内实现了接近衍射极限的偏振无关消色差超透镜设计,但由于其结构特殊,难以实现加工。

收稿日期: 2023-05-18; 修回日期: 2023-06-08; 录用日期: 2023-06-26; 网络首发日期: 2023-09-15

基金项目: 中山市第九批创新科研团队项目(GXTD2022010)、中山市第二批社会公益和基础研究项目(2022B2012)

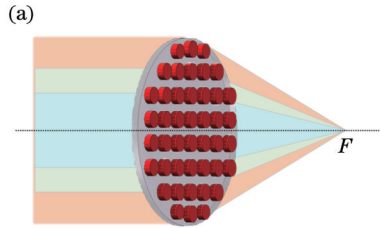
通信作者: *muda@cust.edu.cn

上述研究都是关于可见光波段和近红外波段进行超透镜消色差设计,然而对于中红外波段研究甚少。本文设计的超透镜为全硅介质,设计波段为中红外 3~5 μm ,利用传输相位的原理,实现了尺寸为 37 μm × 37 μm 的消色差超透镜设计。设计的超透镜器件的数值孔径 $NA=0.24$,在正入射的条件下将 3~5 μm 的平面波会聚到轴上的同一焦点,可保持焦距 $f=150 \mu\text{m}$ 不变。

2 宽带消色差超透镜原理及单元结构设计

2.1 宽带消色差超透镜原理

消色差超透镜的聚焦图如图 1(a)所示,一定波段



的入射光经过消色差超透镜后聚焦在同一焦点处。图 1(b)表示入射光从基底一面经过超透镜聚焦在 F 点处,其中 f 为焦距,虚线半圆为球面波前,球面波前与超透镜的交点距透镜中心距离为 r_0 (交点是一个参考位置,该点处的透镜的相位大小为 0)。距中心 r 处的点与球面波前之间的距离为 l 。由于 r_0 处透镜的相位对任意入射光频率都为 0,所以该点的色差最小。将 r_0 的位置设置在透镜的边缘或者边缘以外。

从图 1 中可以分析得到:

$$l = \sqrt{r_0^2 + f^2} - \sqrt{r^2 + f^2}, \quad (1)$$

对应的相位变化为

$$\varphi(r, \omega) = \omega/c(\sqrt{r_0^2 + f^2} - \sqrt{r^2 + f^2}). \quad (2)$$

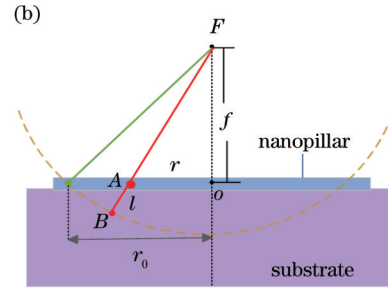


图 1 超透镜原理图。(a)消色差超透镜色散原理图;(b)超透镜聚焦示意图

Fig. 1 Schematic diagram of metalens. (a) Schematic diagram of achromatic metalens dispersion; (b) schematic diagram of metalens focusing

由式(2),以 r_0 处的球面波前为分界, $\varphi(r, \omega)$ 在 r_0 以内关于 ω 斜率为正,与频率 ω 呈正相关; r_0 以外关于 ω 斜率为负,与频率 ω 呈负相关。由于超透镜的结构单元的相位响应随着频率 ω 是线性增大的,即与 ω 是正相关。所以只能调制位置 r_0 以内的透镜的色散,不能调制大于 r_0 的透镜的色散。因此, r_0 决定了透镜的最大半径。

因此聚焦超透镜的相位分布可写为

$$\varphi(r_0, r) = -1/\lambda [2\pi(\sqrt{r_0^2 + f^2} - f)], \quad (3)$$

式中: $r_0 = \sqrt{x^2 + y^2}$ 是超透镜上任意位置 (x, y) 到其中心的距离; f 是焦距。要实现宽带消色差超透镜,在宽波长范围内需要提供焦距保持不变的相位延迟。设 λ_{\max} 和 λ_{\min} 分别是波长的上下边界,一般对于工作波长在 $(\lambda_{\max}, \lambda_{\min})$ 的情况,式(3)可以写为

$$\varphi_{\text{lens}}(R, \lambda) = \varphi_{\text{lens}}(R, \lambda_{\text{lens}}) + \Delta\varphi(R, r), \quad (4)$$

式中,

$$\Delta\varphi(R, r) = -\left(\frac{1}{\lambda} - \frac{1}{\lambda_{\max}\sqrt{R^2 + f^2}}\right). \quad (5)$$

要想实现宽带消色差,不仅要满足参考相位 $\varphi_{\text{lens}}(R, \lambda_{\text{lens}})$,也要满足补偿相位 $\Delta\varphi(R, r)$ 。其中,参考相位与波长 λ 无关,只与 λ_{\max} 有关。然而,补偿相位 $\Delta\varphi(R, r)$ 与波长的倒数即 $1/\lambda$ 线性相关,补偿相位只表示不同波长内的相位差,通过设计不同的单元结构的

传输相位响应来补偿,并非所有的相位响应都和 $1/\lambda$ 线性相关。故引入额外的相位因子 $C(\lambda)$,利用对参数进行优化设计获得相应的相位补偿。由此产生的相位偏移不会对超透镜的聚焦性质产生影响。因此,消色差超透镜的相位剖面可以写为

$$\varphi(R, r) = -\frac{1}{\lambda} [2\pi(\sqrt{R^2 + f^2} - f)] + C(\lambda). \quad (6)$$

式(3)的相位差因此变为

$$\Delta\varphi'(R, r) = \Delta\varphi(R, r) + C(\lambda). \quad (7)$$

2.2 单元结构设计

本文设计的纳米柱结构为全硅介质,硅是常见的红外材料,在 3~5 μm 波段内具有较高的透射率,光损耗很小,可以忽略,且硅材料的超透镜加工工艺比较完备;同时纳米柱结构进行周期性排列,利用传输相位理论通过改变纳米柱的半径引起等效折射率的改变,进而对超透镜的相位进行调控,提供不同位置对应的相位补偿,实现超透镜的消色差功能。

首先设计基底的形状:正方形、六边形,设计纳米结构的形状:圆柱、空心圆柱、长方体。并针对不同形状的单元结构进行仿真,计算单元结构的透过率及相位分布,选择具有较高透过率和能够覆盖 2π 相位分布的形状,最终确定单元结构的形状基底为正方形、纳米结构为具备空间对称性的圆柱,如图 2 所示。图中, H 为单元结构的高度, r 为单元结构的半径, p 为单元结

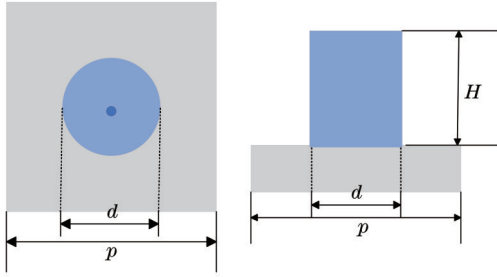


图2 超透镜单元结构示意图

Fig. 2 Schematic diagram of metalens unit structure

构的周期。

增加单元结构的高度能够提高相应的相位变化,但同时也会增加单元结构的深宽比(即 H/d),进而加大加工难度,因此需要平衡高度和相位之间的关系,使相位变化足够大的同时降低单元结构的高度。由于超透镜的加工工艺并不十分完善,选择超透镜的所有纳米柱高度为定值。

通过时域有限差分(FDTD)仿真软件对单元结构的几何参数进行优化,获得不同几何参数单元结构的传输相位,然后利用这些相位、振幅等数据,建立全模设计工作中所需要的数据库。

2.3 透过率及相位分析

本节对单元结构的半径 r 、高度 H 、周期 p 对相位及透过率的影响情况展开分析。通过FDTD法对单元结构进行优化仿真,以此确定能够覆盖 2π 相位且透过率较高的单元结构的半径范围 r 、高度 H 以及周期 p 。

固定单元结构的高度 H 、周期 p ,改变单元结构的半径,得到不同半径对应的相位分布及透过率;固定纳米柱半径 r 及单元结构周期 p ,选取单元结构的高度分别为4、5、6 μm 进行仿真,得到不同单元结构高度的相位分布及透过率;在纳米柱高度 H 和半径 r 保持不变的情况下,选取单元结构周期分别为0.8、1.0、1.2 μm ,得到相应的相位分布及透过率。最终确定单元结构的半径 r 为0.05~0.35 μm 、高度为6 μm 、周期为0.8 μm ,对应9个波长的相位分布和透过率如图3所示,既保证能够实现 2π 的相位覆盖,又保证了结构具备较高的透过率。图3(a)、3(c)、3(e)中横坐标表示纳米柱的半径,纵坐标表示相位延迟,由图可见在设计波长为3~5 μm 时均能够实现 2π 的相位覆盖。图3(b)、3(d)、3(f)中横坐标表示纳米柱半径,纵坐标表示透过率(均在70%以上),通过调整单元结构的半径即可实现对光波进行调控。图3中曲线出现了不平滑节点和相位突变,因为当周期不改变时,纳米柱与纳

米柱之间的距离会影响相位分布,距离较大时,光波通过纳米柱阵列会直接透射,无法进行相位调控;距离较小时,每个纳米柱产生的光场会发生相互作用,对相位产生干扰,无法进行精准的相位调控,导致整体的透过率降低,同时也会降低系统的聚焦效率。

3 仿真结果

超透镜整体半径为37 μm ,仿真的纳米柱半径范围为0.20~0.35 μm ,全波长焦距为147.3 μm ,对半径不同的硅圆柱进行排列,获得实现聚焦功能所需要的微结构阵列。当平面波垂直入射至基底,经过微结构后发现出射光在147.3 μm 处发生了会聚现象,如图4所示。

分别选取波长为3.00、3.25、3.50、3.75、4.00、4.25、4.50、4.75、5.00 μm 绘制离散波长的半峰全宽(FWHM)曲线,如图5所示。通过计算半峰全宽 $F_{\text{WHM}} = \lambda/2NA$ 理论值,图中9个波长的理论衍射极限 F_{WHM} 值分别为6.25、6.77、7.29、7.81、8.33、8.85、9.38、9.90、10.42 μm ,仿真得到的 F_{WHM} 值分别为6.64、6.65、7.32、7.92、8.01、8.93、9.63、10.02、10.65 μm ,计算结果与理论衍射极限具有较好的一致性。

图6中得到了中红外范围(3~5 μm)内圆偏振光正入射条件下的光场分布。其中,图为 y - z 平面的归一化强度分布,实线表示理论焦距 $f=150$ μm 。表1列出了圆偏振光不同入射波长下的焦距值,由此可见,离散波长与全波长焦距值同设计值较为接近,而3.50 μm 和4.00 μm 波长下的焦距与设计值偏差较大。图6清晰地展示了波长分别为3.50、3.75、4.00、4.25、4.50、4.75、5.00 μm 的焦点具有一定的焦深,为40 μm 左右,因此这样的误差几乎可以忽略。而3.00 μm 和3.25 μm 波长的焦深较大,这是由于在此波长下,材料透过率略低。

图7为圆偏振光、X线偏振光、Y线偏振光正入射时不同波长的焦距值曲线,由图中可以看出,三种偏振光入射后焦距值非常接近,说明设计的超透镜结构与偏振无关,这是由于圆柱单元结构的高度空间对称性造成的。

离散波长的聚焦效率如图8所示,其中,聚焦效率为一个艾里斑内聚焦圆偏振光束的光强度与透射光束的光强度之比。图8显示了聚焦效率曲线随工作波长的变化而变化,波长为3.25 μm 时,聚焦效率最低为44.64%,波长为5 μm 时,聚焦效率最高,达到65.2%,聚焦效果良好。在整个工作带宽内聚焦效率约为

表1 圆偏振光下消色差超透镜离散波长的焦距值

Table 1 Focal length values of discrete wavelengths of achromatic metalens under circularly polarized light

Discrete wavelength / μm	3.00	3.25	3.50	3.75	4.00	4.25	4.50	4.75	5.00	All wavelengths
Focal length / μm	149.3	149.0	143.0	141.3	146.1	145.4	141.1	144.7	146.6	147.3

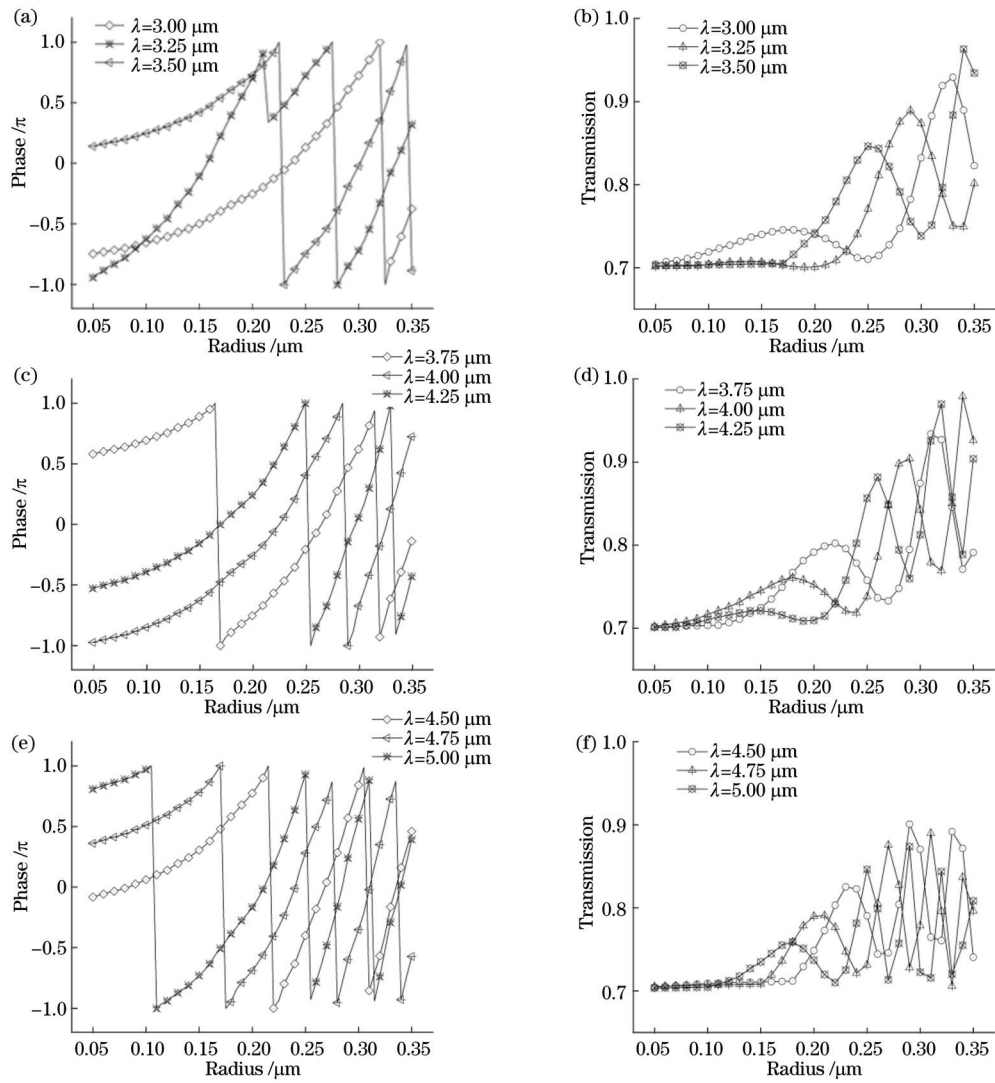


图 3 $r=0.05-0.35 \mu\text{m}$, $H=6 \mu\text{m}$, $p=0.8 \mu\text{m}$ 时单元结构的相位分布及透过率。(a) 波长分别为 3.00、3.25、3.50 μm 时的相位分布; (b) 波长分别为 3.00、3.25、3.50 μm 时的透过率; (c) 波长分别为 3.75、4.00、4.25 μm 时的相位分布; (d) 波长分别为 3.75、4.00、4.25 μm 时的透过率; (e) 波长分别为 4.50、4.75、5.00 μm 时的相位分布; (f) 波长分别为 4.50、4.75、5.00 μm 时的透过率

Fig. 3 Phase distribution and transmission of unit structure with $r=0.05-0.35 \mu\text{m}$, $H=6 \mu\text{m}$, and $p=0.8 \mu\text{m}$. (a) Phase distributions with wavelengths of 3.00, 3.25, and 3.50 μm , respectively; (b) transmission with wavelengths of 3.00, 3.25, and 3.50 μm , respectively; (c) phase distributions with wavelengths of 3.75, 4.00, and 4.25 μm , respectively; (d) transmission with wavelengths of 3.75, 4.00, and 4.25 μm , respectively; (e) phase distributions with wavelengths of 4.50, 4.75, and 5.00 μm , respectively; (f) transmission of wavelengths of 4.50, 4.75, and 5.00 μm , respectively

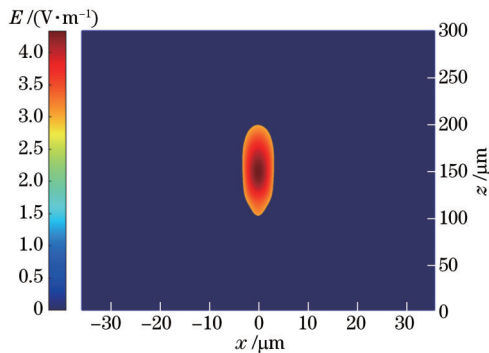


图 4 全波长下消色差超透镜场强图

Fig. 4 Field strength diagram of achromatic metalens at full wavelengths

54%，而这种变化主要是由不同单元结构的相互影响引起的。通过直接优化单元结构的几何参数可以达到聚焦效率较高且均匀的目的。

4 结 论

本文基于传输相位理论设计了一种宽带消色差超透镜,通过设计周期性排列的单元结构,实现了中红外宽带波段的消色差功能。设计的单元结构为全硅介质,通过应用FDTD仿真软件优化单元结构的半径、高度和周期,同时分析了单元结构的不同参数对相位和透过率的影响,确定最终参数值并以此建立单元结构几何参数与相位、振幅响应的数据库。在3~5 μm

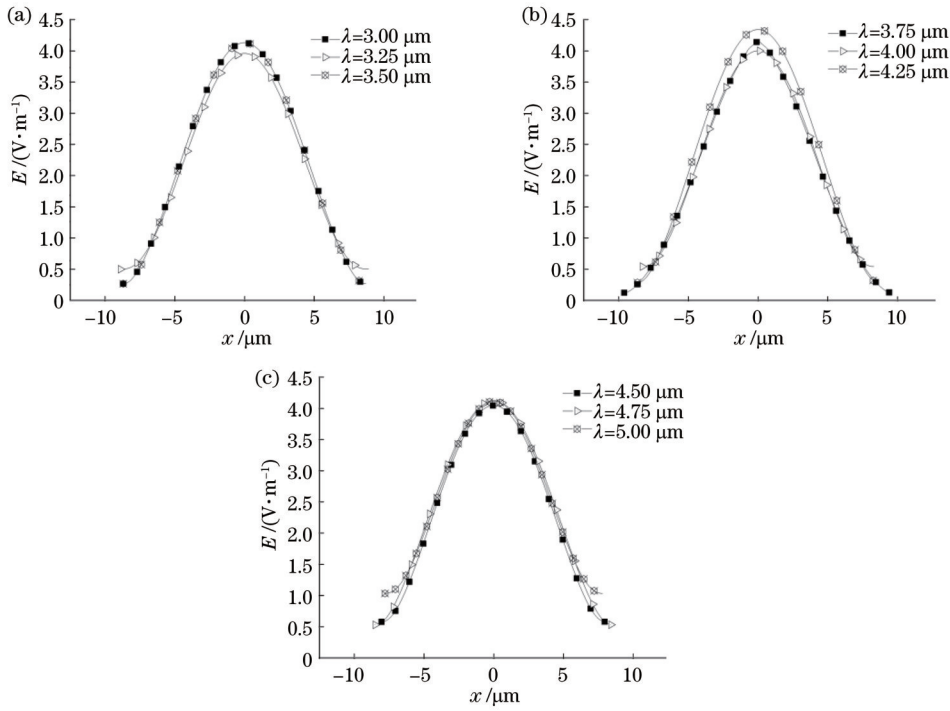


图 5 离散波长的 FWHM 曲线。(a) 波长分别为 3.00、3.25、3.50 μm 时的 FWHM 曲线；(b) 波长分别为 3.75、4.00、4.25 μm 时的 FWHM 曲线；(c) 波长分别为 4.50、4.75、5.00 μm 时的 FWHM 曲线

Fig. 5 FWHM curves of discrete wavelengths. (a) FWHM curves of wavelengths of 3.00, 3.25, and 3.50 μm, respectively. (b) FWHM curves of wavelengths of 3.75, 4.00, and 4.25 μm, respectively. (c) FWHM curves of wavelengths of 4.50, 4.75, and 5.00 μm, respectively

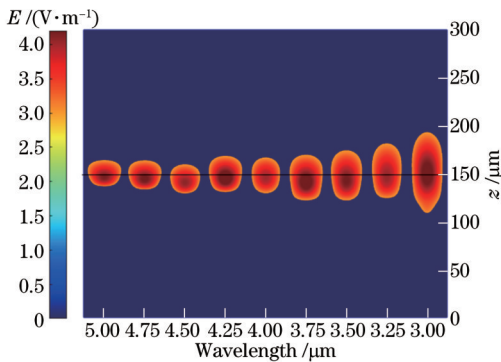


图 6 圆偏振光下离散波长焦点处场强分布

Fig. 6 Field intensity distribution at focuses of discrete wavelengths under circularly polarized light

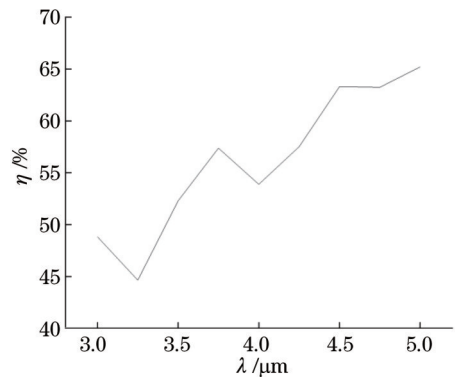


图 8 离散波长的聚焦效率

Fig. 8 Focusing efficiency at discrete wavelengths

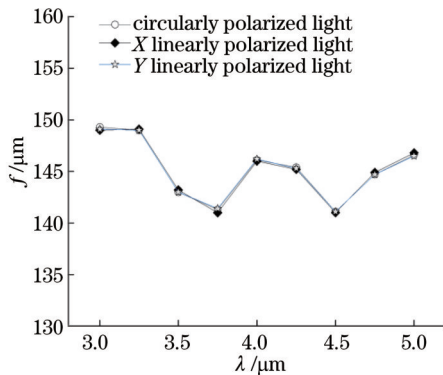


图 7 三种偏振光在不同波长下入射的焦距值曲线

Fig. 7 Focal length curves of three kinds of polarized incident light at different wavelengths

波段实现了消色差聚焦功能,全波长聚焦效率约为 54%。本文提出的宽带消色差超透镜采用的单元结构设计简单,而且不受偏振态的影响,使器件的利用效率有所提高,后续可以引入更多类型的单元结构实现更大带宽的消色差聚焦效果。虽然本文只在中红外区域进行了仿真验证,但该器件的设计原理和方法可以推广到长波红外等其他波段。

参 考 文 献

[1] 任佳慧, 李九生. 基于光敏硅的多功能可重构超表面[J]. 光学学报, 2023, 43(11): 1124003.
Ren J H, Li J S. Multifunctional reconfigurable metasurface based on photosensitive silicon[J]. Acta Optica Sinica, 2023, 43

- (11): 1124003.
- [2] Wu P C, Zhu W M, Shen Z X, et al. Broadband wide-angle multifunctional polarization converter via liquid-metal-based metasurface[J]. *Advanced Optical Materials*, 2017, 5(7): 1600938.
- [3] Wan W W, Gao J, Yang X D. Full-color plasmonic metasurface holograms[J]. *ACS Nano*, 2016, 10(12): 10671-10680.
- [4] Xie X, Pu M B, Li X, et al. Dual-band and ultra-broadband photonic spin-orbit interaction for electromagnetic shaping based on single-layer silicon metasurfaces[J]. *Photonics Research*, 2019, 7(5): 586-593.
- [5] Aieta F, Kats M A, Genevet P, et al. Multiwavelength achromatic metasurfaces by dispersive phase compensation[J]. *Science*, 2015, 347(6228): 1342-1345.
- [6] Arbabi E, Arbabi A, Kamali S M, et al. Multiwavelength polarization-insensitive lenses based on dielectric metasurfaces with meta-molecules[J]. *Optica*, 2016, 3(6): 628-633.
- [7] Avayu O, Almeida E, Prior Y, et al. Composite functional metasurfaces for multispectral achromatic optics[J]. *Nature Communications*, 2017, 8: 14992.
- [8] Li M M, Li S S, Chin L K, et al. Dual-layer achromatic metalens design with an effective Abbe number[J]. *Optics Express*, 2020, 28(18): 26041-26055.
- [9] Wang S M, Wu P C, Su V C, et al. A broadband achromatic metalens in the visible[J]. *Nature Nanotechnology*, 2018, 13(3): 227-232.
- [10] Li Y, Li X, Pu M B, et al. Achromatic flat optical components via compensation between structure and material dispersions[J]. *Scientific Reports*, 2016, 6: 19885.
- [11] Ndao A, Hsu L, Ha J, et al. Octave bandwidth photonic fishnet-achromatic-metalens[J]. *Nature Communications*, 2020, 11: 3205.
- [12] Chen W T, Zhu A Y, Sanjeev V, et al. A broadband achromatic metalens for focusing and imaging in the visible[J]. *Nature Nanotechnology*, 2018, 13(3): 220-226.
- [13] Wang S M, Wu P C, Su V C, et al. Broadband achromatic optical metasurface devices[J]. *Nature Communications*, 2017, 8: 187.
- [14] Balli F, Sultan M A, Ozdemir A, et al. An ultrabroadband 3D achromatic metalens[J]. *Nanophotonics*, 2021, 10(4): 1259-1264.
- [15] Xiong W H, Sha C C, Ding J P. Polarization-independent broadband achromatic metalens in the mid-infrared (3 - 5 μm) region[J]. *Applied Physics Express*, 2022, 15(2): 022001.

Design of Mid-Infrared Broadband Achromatic Metalens

Zhang Yue^{1,2}, Mu Da^{1,2,3*}, Xie Huiyang^{1,2}, Xia Pengyu^{1,2}, Li Tangyue^{1,2,3}, Li Haoxiang^{1,2,3}, Zhang Wenhan^{1,2}

¹Key Laboratory of Optical Control and Optical Information Transmission Technology, Ministry of Education, School of Optoelectronic Engineering, Changchun University of Science and Technology, Changchun 130022, Jilin, China;

²National Demonstration Center for Experimental Opto-Electronic Engineering Education, School of Optoelectronic Engineering, Changchun University of Science and Technology, Changchun 130022, Jilin, China;

³Zhongshan Institute of Changchun University of Science and Technology, Zhongshan 528400, Guangdong, China

Abstract

Objective Metasurfaces are widely employed in planar optics due to their ability to regulate the phase of incident light waves at sub-wavelength sizes, and are now adopted in beam generators, holographic imaging, beam shaping, and other aspects. Meanwhile, metalenses are metasurfaces that can be focused, and the produced light waves are characterized by hyperbolic phases and can provide greater diffraction efficiency than conventional lenses. Unlike traditional lenses that utilize the thickness of the material to achieve spatial focusing, metalens can adjust the phase distribution of incident light in the plane. Additionally, compared with traditional lenses, metalenses can reduce the system volume, and they are easy to integrate into other components. However, in the applications, due to the properties of the material itself, the chromatic aberration will be large, and eliminating the effect of chromatic aberration is essential for the metalens application. Metalens achieves focusing by regulating the phase of incident light, and the varying wavelengths cause changing phase, resulting in chromatic aberration. Since there is no spherical aberration in metalens, chromatic aberration is the most important source of aberration in imaging. More researchers are concentrating on the achromatic metalens design.

Methods We design the metalens structure of all-silicon medium, with the phase modulation of the design band being 3-5 μm . The achromatic metalens design with a size of 37 $\mu\text{m} \times 37 \mu\text{m}$ is realized by the transmission plate principle. The numerical aperture $NA = 0.24$ of the designed metalens device concentrates 3-5 μm plane waves to the same focal point on the axis under the positive incidence, which can keep the focal length $f = 150 \mu\text{m}$ unchanged.

The designed nanopillar structure is an all-silicon medium, and silicon is a common infrared material, with high light transmittance in the 3 - 5 μm band. Meanwhile, the optical loss is very small, which can be ignored, and the metalens processing technology of silicon materials is relatively complete. Additionally, the nanopillar structure is periodically

arranged, and the transmission phase theory is employed to change the equivalent refractive index by varying the nanopillar radius. Then, the metalens phase is regulated, and the phase compensation corresponding to different positions is provided to realize the achromatic function of the metalens (Fig. 2).

Finally, the shape of unit structure is a square substrate, and the nanostructure is a cylinder with spatial symmetry. Increasing the height of the element structure can both augment the corresponding phase change and expend the aspect ratio of the element structure (H/d), thereby increasing the processing difficulty. It is necessary to balance the relationship between height and phase to realize large enough phase change and reduce the height of element structure. Since the processing technology of the metalens is not perfect, the height of all nanopillars of metalens is selected.

The geometric parameters of the unit structure are optimized by finite-difference time-domain (FDTD) simulation software, the transmission phases of the element structure of different geometric parameters are obtained, and then the data such as phase and amplitude are utilized to establish the database required for the full-mode design.

Results and Discussions The height H of the fixed cell structure is $6\ \mu\text{m}$ and the period p is $0.8\ \mu\text{m}$, with the changed radius of the unit structure. Meanwhile, the phase distribution and transmission corresponding to different radii are obtained, and the nanopillar radius is determined to be $0.05\text{--}0.35\ \mu\text{m}$ (Fig. 3). The radius of the fixed nanopillar is $0.05\text{--}0.35\ \mu\text{m}$ and the cell structure period $p=0.8\ \mu\text{m}$. The height of the element structure is selected as 4, 5, and $6\ \mu\text{m}$ for simulation, and the height of the unit structure is determined to be $6\ \mu\text{m}$ during the metalens design. Under the unchanged height H and radius r of the nanopillar, the structural periods of the selected elements are 0.8, 1.0, and $1.2\ \mu\text{m}$ respectively, and the period is determined to be $0.8\ \mu\text{m}$. This ensures the phase coverage of 2π and the high transmission of the structure.

This shows the focal length curves of different wavelengths when circularly polarized light, X -linearly polarized light, and Y -linearly polarized light are normal incident (Fig. 7). The figure on the right reveals that the focal length values of the three polarized lights are very close, indicating the consistent designed metalens structure. The polarization is independent due to the high spatial symmetry of the cylindrical cell structure.

The focusing efficiency is the ratio of the light intensity of the focused circular polarized beam in an Airy spot to the light intensity of the transmitted beam. It is shown that the focusing efficiency curve changes with varying working wavelengths (Fig. 8). The lowest focusing efficiency is 44.64% under the wavelength of $3.5\ \mu\text{m}$, and the highest focusing efficiency is 65.2% under the wavelength of $5\ \mu\text{m}$, with sound focusing effect. The focusing efficiency is about 54% over the entire operating bandwidth, and this change is mainly caused by the interaction between different cell structures. The geometric parameters (p and H) of element structure are optimized to achieve high and uniform focusing efficiency.

Conclusions We design a broadband achromatic metalens, which employs the transmission phase theory and the periodic arrangement of the unit structure to realize the dispersion control of the mid-infrared broadband. The designed element structure is an all-silicon medium, and the geometric parameters of the unit structure are optimized by FDTD commercial simulation software. Meanwhile, the influence of different parameters of the element structure on phase and transmission is analyzed, and a database of the geometric parameters and phase and amplitude response of the nanopillar is established. The achromatic focusing function is realized in the $3\text{--}5\ \mu\text{m}$ band, and the full-wavelength focusing efficiency is about 54%. The proposed unit structure of the broadband achromatic metalens is simple and not affected by the polarization state, improving the utilization efficiency of the device. Subsequently, more types of cell structures can be introduced to achieve an achromatic focusing effect with larger bandwidths, which has certain application prospects in color display imaging systems. Although we only perform simulation verification in the visible region, the design principles and methods of the device can be generalized to other bands such as long-infrared bands.

Key words metalens; mid-infrared band; planar lens; achromatism; broadband